The effect of lattice models within the lattice Boltzmann method in the simulation of wall-bounded turbulent flows

Shin K. Kang *, Yassin A. Hassan

Department of Nuclear Engineering, Texas A&M University, College Station, TX 77843-3133, USA

ABSTRACT

This study investigated the effect of 3D lattice models (D3Q19 and D3Q27 lattices) on the simulation results of wall-bounded turbulent flows in a circular pipe and in a square duct. The LES with the Smagorinsky subgrid-scale (SGS) model was adopted for the turbulence simulation. To improve the credibility of our results on the lattice model effect, a comprehensive sensitivity study was performed of boundary treatment techniques and collision models, as well as grid sizes in the simulation of the turbulent pipe flows. Through the turbulent circular pipe flow simulation, it was discovered that the D3Q27 lattice model could achieve the rotational invariance in terms of long-time-averaged turbulence statistics and generated the results comparable to the DNS data, while the D3Q19 lattice model broke the rotational invariance and produced unreasonable data. In the turbulent square duct flow simulation, the rotational invariance was evaluated by comparing the results before and after rotating the geometry by 45° about a center. As in the circular pipe flow simulation, the D3Q19 lattice model could not achieve the rotational invariance while the D3Q27 lattice model could. The D3Q19 lattice model also produced poor results compared to those from the D3Q27 lattice model. These defects of the D3Q19 lattice model could be explained by the planes consisting of 2D lattices with five velocities (called defective planes in this study) in the D3Q19 lattice model, based on White and Chong's [14] hypothesis. The defective planes had a deficiency in the momentum transfer of flow and turbulence, thus breaking the rotational invariance and causing the inaccurate results for tested problems.

© 2012 Published by Elsevier Inc.

1. Introduction

In recent years, simulations of the wall-bounded turbulent flows using the lattice Boltzmann method (LBM) have been widely performed. Most researchers have used the direct numerical simulation (DNS) [1–3] or the large eddy simulation (LES) [4–8] as turbulence models in their lattice Boltzmann calculations because other turbulence models based on Reynolds-averaged-Navier–Stokes (RANS) equations are not effective in the LBM with the isotropic cubic lattice. For the lattice model in the turbulence simulation, the D3Q19 lattice model was mainly adopted [1–9] because it produces more accurate and stable results than the D3Q15 lattice model [9,10], and has the comparable accuracy with the DNS and better efficiency in terms of memory and CPU time than the D3Q27 lattice model. For the collision models in the lattice Boltzmann equation (LBE), the single-relaxation-time (SRT) model [1–3,8] and the multiple-relaxation-time (MRT) model [1,3–7], which has better stability than the SRT model [11], were mainly employed.

---

* Corresponding author. Tel.: +1 979 845 7090; fax: +1 979 845 6443.
  E-mail address: paengki1@tamu.edu (S.K. Kang).

Specifically, Lammers et al. [2] used the DNS turbulence model within the incompressible D3Q19 SRT-LBE to simulate the turbulent plane-channel flow (Re$_\tau$ = 180). Their results showed good agreement with those from their pseudo-spectral method and previous DNS data. Premnath and his colleagues [5–7] coupled the various LES turbulence models – Smagorinsky SGS model [5,7], dynamic SGS eddy viscosity model, and dynamic mixed model [6] – with D3Q19 MRT-LBE with an external forcing term. Their models produced results comparable to the DNS data for the typical turbulent plane-channel flows [6,7] and the turbulent square duct flows [5]. Jafari and Rahnama [4] coupled the shear-improved Smagorinsky model (SISM) with the D3Q19 MRT-LBE of Premnath et al. [7] to simulate the turbulent channel flow. Weickert et al. [8] included the WALE SGS model in the D3Q19 MRT-LBE to simulate the turbulent channel flow (Re$_\tau$ = 395) and flow past a wall-mounted cube in the channel. Bespalko et al. [1] performed the DNS within the D3Q19 MRT-LBE (but without tuning the relaxation time) to simulate fully-developed turbulent channel flows (Re$_\tau$ = 180). Freitas et al. [3] performed the comparative study of D3Q19 SRT-LBE, D3Q27 SRT-LBE, D3Q19 MRT-LBE, and the D3Q19 cascaded LBE (CLBE) [12]. In the simulation of turbulent plane-channel flows, they found that the stability and accuracy of the advanced-moment-based schemes like the MRT-LBE and CLBE are not necessarily better than non-moment-based schemes, such as D3Q19 and D3Q27 SRT-LBEs.

However, to the best of the authors' knowledge, an application of LBM turbulence models to the turbulent pipe flow has not yet been examined. This may be because the D3Q19 lattice model, which is typically adopted in the 3D LBM simulation, fails to produce results comparable to the reference DNS data [13]. This was confirmed by our preliminary calculations using the D3Q19 lattice model. The detailed results will be delivered in the Section 3. In addition, the preliminary calculation showed that the D3Q27 lattice model could produce results comparable to the DNS data. It should also be pointed out that, although the flow geometry is different from the circular pipe flow, Meyer and Hazi [9] showed that D3Q19 model could not properly simulate the turbulent flow in a triangularly arrayed rod bundle, while the D3Q27 model could.

On the other hand, the recent work of White and Chong [14] showed that the rotational invariance was broken when using the D3Q19 lattice model for the laminar flow in an axisymmetrical tube with a smooth contraction and an abrupt expansion, although the rotational invariance is maintained for laminar flows in a straight pipe. They explained it using the hypothesis that the breaking of the rotational invariance in the D3Q19 lattice model is due to the lack of velocity vectors in certain planes (called the defective planes in this study), causing parts of the solution to be inadequately resolved. They also showed that the D3Q27 lattice model, whose lattice has the nine velocities for the planes, could resolve the problem.

In the present paper, we show that the unreasonable simulation results of turbulent pipe flows under the D3Q19 lattice model are due to the same reason, i.e., the effect of the defective planes, as in the White and Chong's hypothesis [14] and that the D3Q27 lattice model without such planes can produce the turbulence statistics comparable to the DNS data for the same problem. In addition, simulating the square duct flows with, and without, geometry rotation by 45°, we show that the effect of the defective planes under the D3Q19 lattice model is also critical in the simulation of other wall-bounded turbulent flows.

The remaining part of this paper is organized as follows. In Section 2, the numerical methods adopted in this study are described. The lattice Boltzmann equation, solid wall boundary treatment techniques, and the LES turbulence model in the LBM are covered in this section. In Section 3, the solid wall boundary treatment is first verified in the laminar circular pipe flow, and the simulation results of the turbulent circular pipe flows are provided. The simulation results of the turbulent flows in a square duct with and without 45° rotation are addressed in Section 4. In Section 5, the results are analyzed, and the important things obtained from this study are discussed. Finally, in Section 6, the summary and conclusions of this study are provided.

2. Numerical methods

2.1. Lattice Boltzmann method (LBM)

The single-relaxation-time lattice Boltzmann equation (SRT LBE) with an external forcing term can be expressed as [15]:

$$f_\alpha(\mathbf{x} + \mathbf{e}_\alpha \Delta t, t + \Delta t) = f_\alpha(\mathbf{x}, t) - \frac{1}{\tau}\left[f_\alpha(\mathbf{x}, t) - f_\alpha^{(eq)}(\mathbf{x}, t)\right] + \left(1 - \frac{1}{2\tau}\right)S_\alpha(\mathbf{x}, t)\Delta t, \tag{1}$$

where $f_\alpha(\mathbf{x}, t)$ is the density distribution function for the discrete velocity vector $\mathbf{e}_\alpha$ in the αth direction at position $\mathbf{x}$, and time t and τ is non-dimensional relaxation time. The last term in the right hand side (RHS) of Eq. (1) represents the external force effect to describe the pressure gradient force in this study.

For the equilibrium density distribution function $f_\alpha^{(eq)}$, we adopt the incompressible model [2,16]:

$$f_\alpha^{(eq)} = w_\alpha \left\{ \rho + \rho_0 \left[u_i \frac{e_{\alpha i}}{c_s^2} + u_i u_j \frac{e_{\alpha i} e_{\alpha j} - c_s^2 \delta_{ij}}{2c_s^4} \right] \right\}, \tag{2}$$

where subscripts i and j are Cartesian tensor indices, δ_{ij} is the Kronecker delta, c_s is the speed of sound, and ρ_0 is the reference density. The discrete forcing term $S_\alpha(\mathbf{x}, t)$ can be expressed as:

$$S_\alpha = w_\alpha \left[F_i \frac{e_{\alpha i}}{c_s^2} + (u_i F_j + u_j F_i) \frac{e_{\alpha i} e_{\alpha j} - c_s^2 \delta_{ij}}{2c_s^4} \right]. \tag{3}$$

Then, the density, velocity, and force density can be determined by:

$$\rho = \sum_\alpha f_\alpha, \tag{4a}$$

$$\rho_0 u_i = \sum_\alpha e_{\alpha i} f_\alpha + \frac{\Delta t}{2} F_i, \tag{4b}$$

and

$$F_i = \sum_\alpha e_{\alpha i} S_\alpha. \tag{4c}$$

Using the Chapman-Enskog multi-scale analysis, one can show that the LBE (Eq. (1)) recovers continuity and Navier–Stokes equations with second-order accuracy [15]. During this process, the kinematic viscosity is defined by:

$$v = \frac{1}{3} c^2 \left(\tau - \frac{1}{2}\right) \Delta t. \tag{5}$$

2.1.1. 3D Lattice models in the LBM

In this study, we consider the 19- and 27-velocity models on a 3D cubic lattice, denoted as the D3Q19 and D3Q27 lattice models, respectively. In the D3Q19 and D3Q27 lattice models, discrete velocity vectors $\mathbf{e}_\alpha$ are defined by:

$$\mathbf{e}_\alpha = \begin{cases} (0,0,0), & \alpha = 0, \\ c(\pm1,0,0), c(0,\pm1,0), c(0,0,\pm1), & \alpha = 1,2,\ldots,6, \\ c(\pm1,\pm1,0), c(\pm1,0,\pm1), c(0,\pm1,\pm1), & \alpha = 7,8,\ldots,18 \end{cases} \tag{6a}$$

and

$$\mathbf{e}_\alpha = \begin{cases} (0,0,0), & \alpha = 0, \\ c(\pm1,0,0), c(0,\pm1,0), c(0,0,\pm1), & \alpha = 1,2,\ldots,6, \\ c(\pm1,\pm1,0), c(\pm1,0,\pm1), c(0,\pm1,\pm1), & \alpha = 7,8,\ldots,18, \\ c(\pm1,\pm1,\pm1), & \alpha = 19,20,\ldots,27, \end{cases} \tag{6b}$$

respectively, and the corresponding weighting coefficients w_α are

$$w_\alpha = \begin{cases} 1/3, & \alpha = 0, \\ 1/18, & \alpha = 1,2,\ldots,6, \\ 1/36, & \alpha = 7,8,\ldots,18 \end{cases} \tag{7a}$$

and

$$w_\alpha = \begin{cases} 8/27, & \alpha = 0, \\ 2/27, & \alpha = 1,2,\ldots,6, \\ 1/54, & \alpha = 7,8,\ldots,18, \\ 1/216, & \alpha = 19,20,\ldots,27, \end{cases} \tag{7b}$$

respectively. Here, the lattice speed is $c = \Delta x/\Delta t$, where Δx and Δt are the grid size and the time step size, respectively.

Fig. 1 shows the D3Q19 and D3Q27 lattice models. The fundamental difference between two lattice models is that the D3Q19 lattice model has only five velocity vectors (including $\mathbf{e}_0$) on certain diagonal planes (e.g., the diagonal plane bisecting the 1st and 3rd quadrants of xy-plane contains $\mathbf{e}_0$, $\mathbf{e}_5$, $\mathbf{e}_6$, $\mathbf{e}_7$, and $\mathbf{e}_{10}$ velocity vectors), whereas the D3Q27 lattice model has nine velocity vectors (e.g. the diagonal plane above contains $\mathbf{e}_0$, $\mathbf{e}_5$, $\mathbf{e}_6$, $\mathbf{e}_7$, $\mathbf{e}_{10}$, $\mathbf{e}_{19}$, $\mathbf{e}_{22}$, $\mathbf{e}_{23}$, and $\mathbf{e}_{26}$).

2.1.2. Solid boundary treatment techniques

Since the solid boundary does not match computational nodes in the circular pipe (discussed in Section 3) and 45°-rotated square duct (discussed in Section 4), a solid boundary treatment is required to obtain a better accuracy than the conventional bounce-back scheme without interpolation. In this study, we adopt the Yu et al.'s second-order linear interpolation scheme [17], which reads:

$$f_{\alpha'}^*(\mathbf{x}_w, t) = \frac{\Delta}{1+\Delta} f_\alpha^*(\mathbf{x}_f, t) + \frac{1-\Delta}{1+\Delta} f_\alpha^*(\mathbf{x}_{ff}, t) + \frac{\Delta}{1+\Delta} f_{\alpha'}^*(\mathbf{x}_f, t), \tag{8}$$

where $\mathbf{e}_{\alpha'} = -\mathbf{e}_\alpha$; f_α^* and $f_{\alpha'}^*$ indicate the post-collision density distribution function in $\mathbf{e}_\alpha$ and $\mathbf{e}_{\alpha'}$ directions, $\mathbf{x}_w$ is the node inside the solid linked to the fluid node by $\mathbf{e}_{\alpha'}\Delta t$, $\mathbf{x}_b$ is the intersection of the link and the solid boundary, $\mathbf{x}_f = \mathbf{x}_w + \mathbf{e}_{\alpha'}\Delta t$; $\mathbf{x}_{ff} = \mathbf{x}_w + 2\mathbf{e}_{\alpha'}\Delta t$, and $\Delta = |\mathbf{x}_f - \mathbf{x}_b|/|\mathbf{x}_f - \mathbf{x}_w|$ (see Fig. 2). It should be pointed out that this scheme can be consistently applied
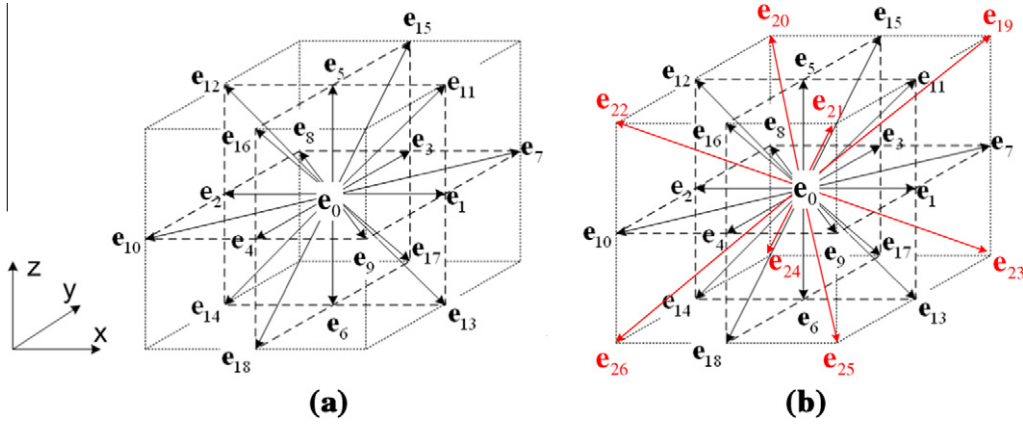
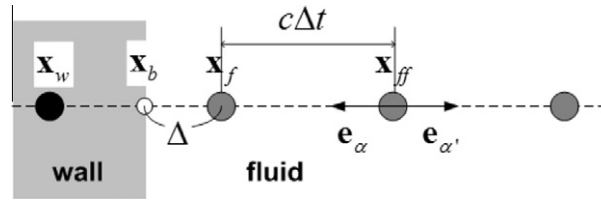**Fig. 1.** (a) D3Q19 and (b) D3Q27 lattice models.

Fig. 2. Node identification in the solid boundary treatment.

to the geometry with periodic boundary conditions because the RHS in Eq. (8) only requires $f_\alpha^*(\mathbf{x}_{ff}, t)$ which can be obtained directly from the periodic boundary condition.

For comparison, the following conventional first-order bounce-back scheme without interpolation is also considered for the cylinder pipe problem in this study.

$$f_{\alpha'}^*(\mathbf{x}_w, t) = f_\alpha^*(\mathbf{x}_f, t). \tag{9}$$

For the square duct flow, we employ the halfway bounce-back scheme, where we locate the boundary at the center between $\mathbf{x}_w$ and $\mathbf{x}_f$, and then use Eq. (9).

2.2. Turbulence models

In this study, we use the LES turbulence approach with Smagorinsky subgrid-scale (SGS) model for the turbulence simulation.

2.2.1. LES turbulence model in the LBM
The filtered lattice Boltzmann equation (LBE) can be expressed as:

$$\bar{f}_\alpha(\mathbf{x} + \mathbf{e}_\alpha \Delta t, t + \Delta t) = \bar{f}_\alpha(\mathbf{x}, t) - \frac{1}{\tau^*}\left[\bar{f}_\alpha(\mathbf{x}, t) - \bar{f}_\alpha^{(eq)}(\mathbf{x}, t)\right] + \left(1 - \frac{1}{2\tau^*}\right)\bar{S}_\alpha(\mathbf{x}, t)\Delta t, \tag{10}$$

where overbars are used to indicate the filtered values. This equation is exactly the same form as the conventional LBE (Eq. (1)), but the density distribution functions and discrete forcing terms are replaced by their filtered values. In addition, the relaxation time becomes the total relaxation time (τ^*) defined as $\tau^* = \tau + \tau_t$ corresponding to the total viscosity (v^*) as:

$$v^* = v + v_t = \frac{1}{3}\left(\tau^* - \frac{1}{2}\right)c^2\Delta t = \frac{1}{3}\left(\tau + \tau_t - \frac{1}{2}\right)c^2\Delta t, \tag{11}$$

where the turbulent viscosity (v_t) is determined by turbulent relaxation time (τ_t) defined as:

$$v_t = \frac{1}{3}\tau_t c^2\Delta t. \tag{12}$$

2.2.2. Smagorinsky SGS model
The turbulent stress in the eddy viscosity SGS model can be written as:

$$\tau_{ij}^t - \frac{1}{3}\delta_{ij}\tau_{kk}^t = -2v_t\bar{S}_{ij}. \tag{13}$$

In the Smagorinsky SGS model, the turbulence eddy viscosity v_t can be expressed as:

$$v_t = (C_S \Delta)^2 |\bar{S}|,\tag{14}$$

where C_S is a Smagorinsky constant, and we use $C_S = 0.1$ in this study. Also, the filtered strain rate is defined as:

$$|\bar{S}| = \sqrt{2\bar{S}_{ij}\bar{S}_{ij}}\tag{15}$$

with the filtered strain rate tensor

$$\bar{S}_{ij} = \frac{1}{2}\left(\frac{\partial \bar{u}_i}{\partial x_j} + \frac{\partial \bar{u}_j}{\partial x_i}\right).\tag{16}$$

In general, to avoid the over-damping near the wall, van Driest damping is included in Eq. (14). The resulting Smagorinsky SGS model with van Driest damping reads:

$$v_t = [C_S \Delta (1 - e^{-y^+/A^+})]^2 |\bar{S}|,\tag{17}$$

where Δ is the filter size and is equal to the grid size Δx; $y^+ = u_\tau y/v$; and $A^+ = 25$ [18]. Here, y is the wall-normal distance and the friction velocity $u_\tau \equiv \sqrt{\tau_w/\rho}$ where τ_w is the wall shear stress.

In the LBM, the components of the filtered strain rate tensor can be locally expressed without involving any additional finite difference calculations by using the second moment of the filtered non-equilibrium density distribution functions; i.e., the filtered non-equilibrium momentum flux tensor, as

$$\bar{S}_{ij} = -\frac{1}{2\Delta t \tau^* \rho c_s^2}\bar{Q}_{ij}\tag{18}$$

with

$$\bar{Q}_{ij} \equiv \bar{\Pi}_{ij}^{(neq)} + 0.5(\bar{u}_i \bar{F}_j + \bar{u}_j \bar{F}_i),\tag{19}$$

where the filtered non-equilibrium momentum flux tensor is determined by

$$\bar{\Pi}_{ij}^{(neq)} = \sum_\alpha e_{\alpha i} e_{\alpha j} (\bar{f}_\alpha - \bar{f}_\alpha^{(eq)}).\tag{20}$$

Then, from Eqs. (11), (12), (15), (17)–(20) we can directly obtain:

$$\tau^* = \tau + \tau_t = \frac{1}{2}\left(\tau + \sqrt{\tau^2 + \frac{18\sqrt{2}[C_s \Delta(1 - e^{-y^+/A^+})]^2 \sqrt{\bar{Q}_{ij}\bar{Q}_{ij}}}{\rho \Delta t^2 c^4}}\right).\tag{21}$$

3. Turbulent flows in a circular pipe

We start with turbulent circular pipe flows because we can test the effect of lattice models, i.e., the effect of the defective planes, without rotating the geometry due to its axisymmetry. First, for the convenience of the explanation, we define the Planes D1, D2, V, and H as can be seen in Fig. 3. This figure also depicts unit lattice constituting each plane. Here, the red vectors are only valid for the D3Q27 lattice model.

3.1. Laminar circular pipe flows

In wall-bounded turbulent flows, the wall boundaries, in general, do not match with computational nodes. To impose the no-slip boundary condition in such conditions, we adopt Yu et al.'s linear interpolation scheme [17] and the bounce-back scheme for reference as mentioned in Section 2.1.2. In this section, these boundary treatment techniques are verified using the analytical solution for the laminar flow in a circular pipe.

In the simulation, we consider a pipe with a diameter D and a length $2D$. For the inlet and outlet flow boundaries, the periodic inlet–outlet boundary condition with an external force density term corresponding to the pressure gradient is imposed. The Reynolds number of the flow is set to $Re_D = Du_{avg}/v = 500$, where u_{avg} is the average streamwise velocity. In this flow condition, we perform the grid sensitivity study with Yu et al.'s scheme and the bounce-back scheme under both D3Q19 and D3Q27 lattice models. Here, the accuracy of each method set is evaluated by L_2- and L_∞-errors defined as:

$$L_2\text{-error} \equiv \sqrt{\frac{1}{N}\sum_{i,j}^{N}\left(\frac{u_z - u_{z,analytic}}{u_{z,analytic}}\right)^2},\tag{22a}$$

$$L_\infty\text{-error} \equiv \max_{i,j}\left|\frac{u_z - u_{z,analytic}}{u_{z,analytic}}\right|,\tag{22b}$$
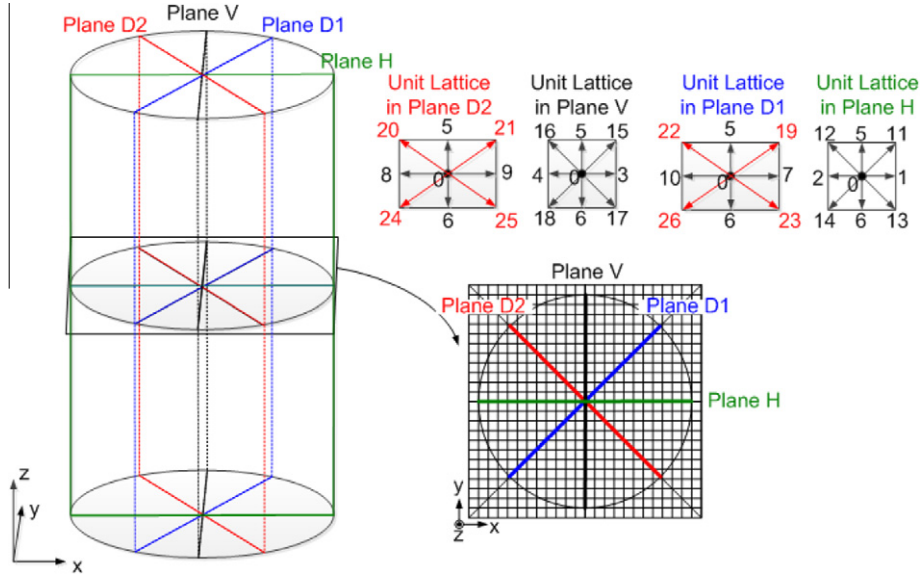
Fig. 3. Definition of *Planes V*, *H*, *D1*, and *D2* and unit lattices on these planes in the pipe geometry.

respectively. Here, u_z and $u_{z,analytic}$ are calculated, and analytical streamwise velocities at nodes (i,j) on a cross-sectional plane, respectively, and N is total number of the nodes in the cross-sectional plane.

Fig. 4 shows the L_2- and L_∞-errors obtained from different solid boundary treatments in the D3Q19 and D3Q27 lattice models. We used three grid size levels; i.e., $\Delta x = D/20$, $D/40$, and $D/80$ for the D3Q27 model and $\Delta x = D/30$, $D/40$, and $D/80$ for the D3Q19 model. For the D3Q19 model, instead of $\Delta x = D/20$, $\Delta x = D/30$ was used as the coarsest grid level because the result obtained from $\Delta x = D/20$ in the D3Q19 lattice model was not in the asymptotic range of convergence in the preliminary calculation. For both lattice models, orders of grid convergences of Yu et al.'s scheme and the bounce-back scheme are close to 2 and 1, respectively, for both L_2- and L_∞-errors, as expected. It should also be pointed out that the nodes corresponding to L_∞-errors are not located on the *Planes D1* and *D2*.

3.2. Turbulent pipe flows

Now, we consider the turbulent flows in a circular pipe. The flow condition is Re_τ ($=u_\tau D/v$) = 360, where D is the pipe diameter, and the pipe length is set to be $5D$, as in [13]. For the inlet and outlet boundaries, the periodic boundary condition is used. For the solid boundaries, no slip boundary conditions are imposed by using Yu et al.'s scheme and bounce-back
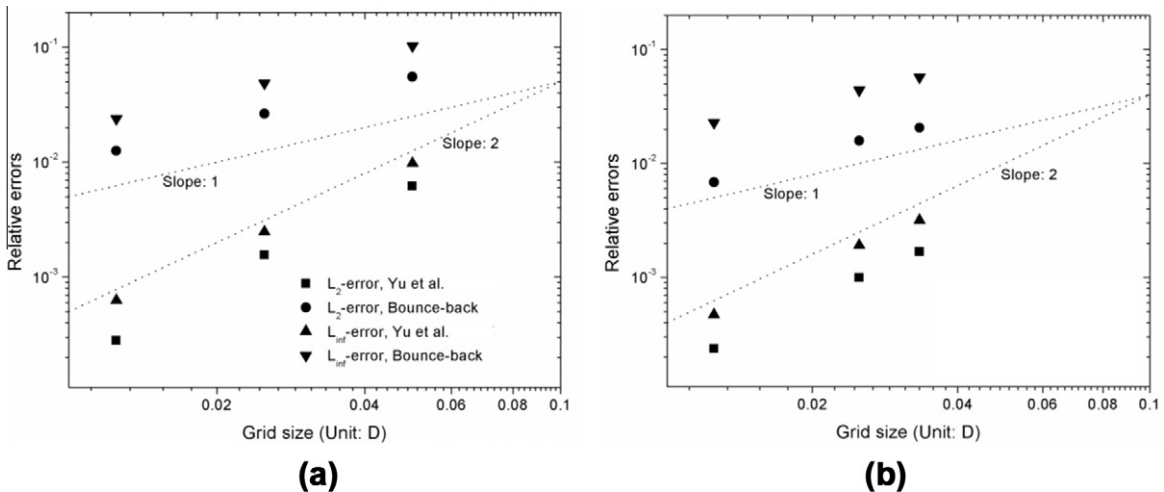

Fig. 4. L_2- and L_∞-errors of Yu et al.'s scheme and the bounce-back scheme under (a) the D3Q27 lattice model and (b) the D3Q19 lattice model.

schemes. As in the laminar pipe flow simulation, a constant pressure gradient is included in the flow equation as an external source term using $\bar{\tau}_w = \rho_0 u_\tau^2 = -\frac{1}{4} D \frac{dP}{dz}$. The Smagorinsky SGS model (with $C_S = 0.1$) with van Driest damping is adopted for the turbulence.

The turbulence statistics are obtained from time-averaging over $10t^*$ ($=D/u_\tau$) after the flow reaches a statistically steady state, which is identified by a linear profile of the total shear stress [19]. The radial profiles are calculated by averaging the time-averaged values over the streamwise direction and then over circumferential directions at the same radial position. The DNS data of Eggels et al. [13] are used as reference data. In the presentation of the results, y^+ is defined as $y^+ \equiv D^+/2 - r^+$ where r is the radial coordinate in the cylindrical coordinate system with a pipe center as an origin. The velocity and the root-mean-square (RMS) velocity are normalized by the friction velocity u_τ.

We start with results obtained from the D3Q27 lattice model. Fig. 5 presents the results of grid sensitivity study with four levels of grid sizes $\Delta x = D/48$, $D/60$, $D/72$, and $D/100$. The upper three levels ($D/60$, $D/72$, and $D/100$) produce results comparable to the DNS data. In contrast, with grid size $\Delta x = D/48$, the streamwise mean velocity is under-estimated in the overall y^+ range and approaching to the center, the RMS velocities attenuate less, and disperse more, than those from higher grid resolutions and DNS. In addition, near the wall (i.e., in the viscous sublayer and the buffer layer) the streamwise mean velocities and the RMS velocities obtained from $\Delta x = D/60$ ($\Delta x^+=6$) are still slightly under-predicted due to the coarse resolution, whereas with $\Delta x = D/100$ ($\Delta x^+ = 3.6$), the data are located on the DNS data curve.

The turbulence statistics obtained even for quite a long time cannot be perfectly rotationally invariant due to the nature of turbulence. Thus, if with changing radial positions, quite different circumferential locations are involved in the averaging process as in the Cartesian grid, their radial profiles may intrinsically have some discontinuity; i.e., fluctuation. This is in contrast to the general body-conformal grid, or the structured grid based on the cylindrical coordinate, where, at a radial position, numerous isotropically-located points are involved during the averaging process, thus producing relatively smooth radial profiles. In the simulation of the turbulent circular pipe flow with the grid size of $\Delta x = D/72$, for example, at consecutive $y^+ = 39.91$, 40, and 40.54, the number of nodes involved in the average are 16, 4, and 8, and corresponding azimuthal angles are $(0 \pm 2.05, 45 \pm 10.18, 90 \pm 2.05, 135 \pm 10.18, 180 \pm 2.05, 225 \pm 10.18, 270 \pm 2.05, 315 \pm 10.18)$, $(0, 90, 180, 270)$, $(0 \pm 14.53, 90 \pm 14.53, 180 \pm 14.53,$ and $270 \pm 14.53)$ in the unit of degree, respectively. In spite of the intrinsic property of the Cartesian grid and the nature of the turbulence, the fluctuations of the radial turbulence profiles are small in the D3Q27 lattice model, which reflects the rotational invariance of the D3Q27 lattice model in terms of long-time-averaged turbulence statistics.

Fig. 6 shows the effect of solid boundary treatments under the grid size $\Delta x = D/60$. The bounce-back scheme under-predicts the streamwise mean velocity by 2% in the overall y^+ range, while the turbulent fluctuation velocities are similar to Yu et al.'s scheme. The data below the buffer layer are slightly more dispersed compared to that of Yu et al.'s scheme due to the staircase-shaped boundary in the bounce-back scheme.

Now, we move on into the D3Q19 lattice model. Fig. 7 presents the streamwise mean velocities and the RMS velocities under the D3Q19 lattice model. This figure contains effects of boundary treatments (red lines) and collision operators (blue lines), as well as grid resolution (dark cyan lines) against the standard case with Yu et al.'s scheme (black lines).

Under the standard case (black lines), all the profiles have large fluctuations near the wall, and closer to the center, the fluctuations become smaller. The streamwise mean velocity is under-estimated (about 28% lower than the DNS data at the center), except for some radial positions near the wall. This kind of under-estimation of the streamwise velocity was also observed in White and Chong's case [14], where under the D3Q19 lattice model, the isotropy between Planes D1 and D2 and Planes V and H was broken just downstream of the sudden expansion, and the centerline streamwise velocity was lowered over 10% compared to the D3Q27 lattice model.
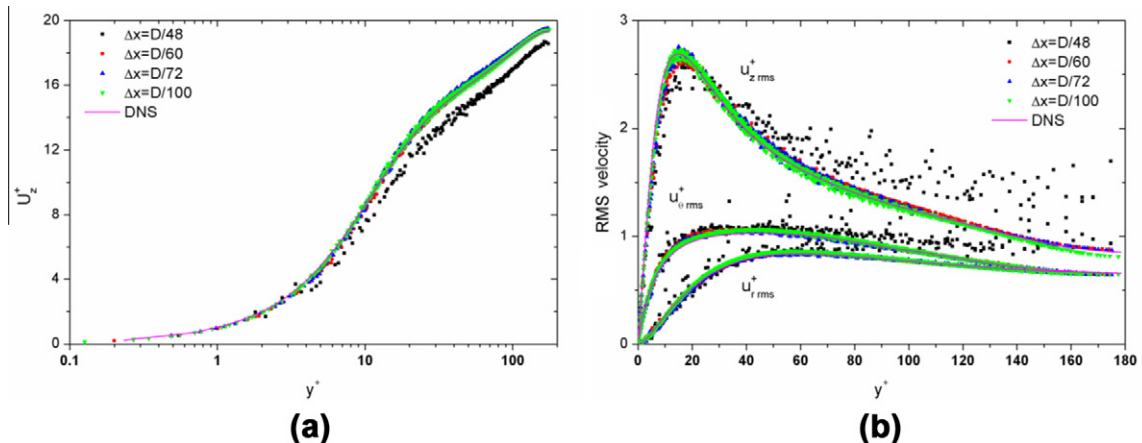

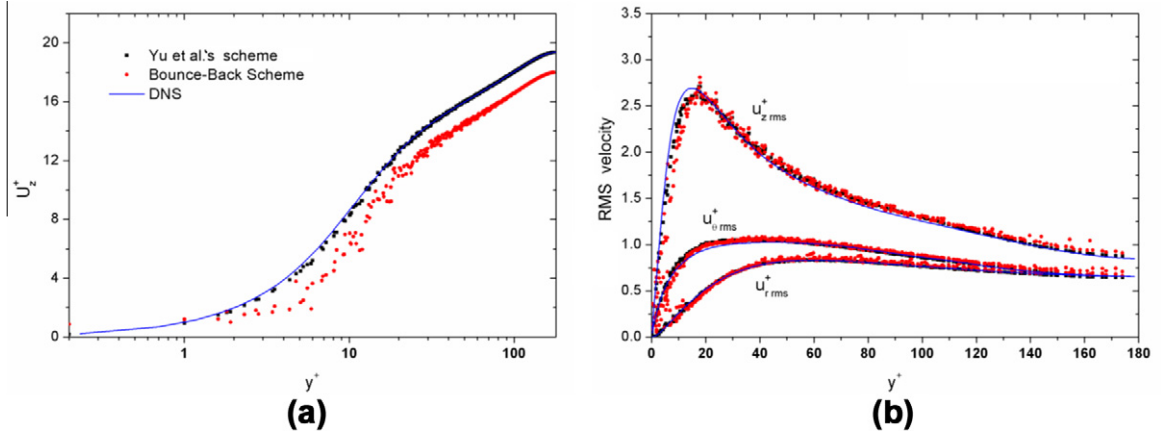**Fig. 5.** (a) Streamwise mean velocities and (b) RMS fluctuation velocities for different grid sizes.

Fig. 6. Comparison of solid boundary treatment techniques: (a) streamwise mean velocities and (b) RMS fluctuation velocities.
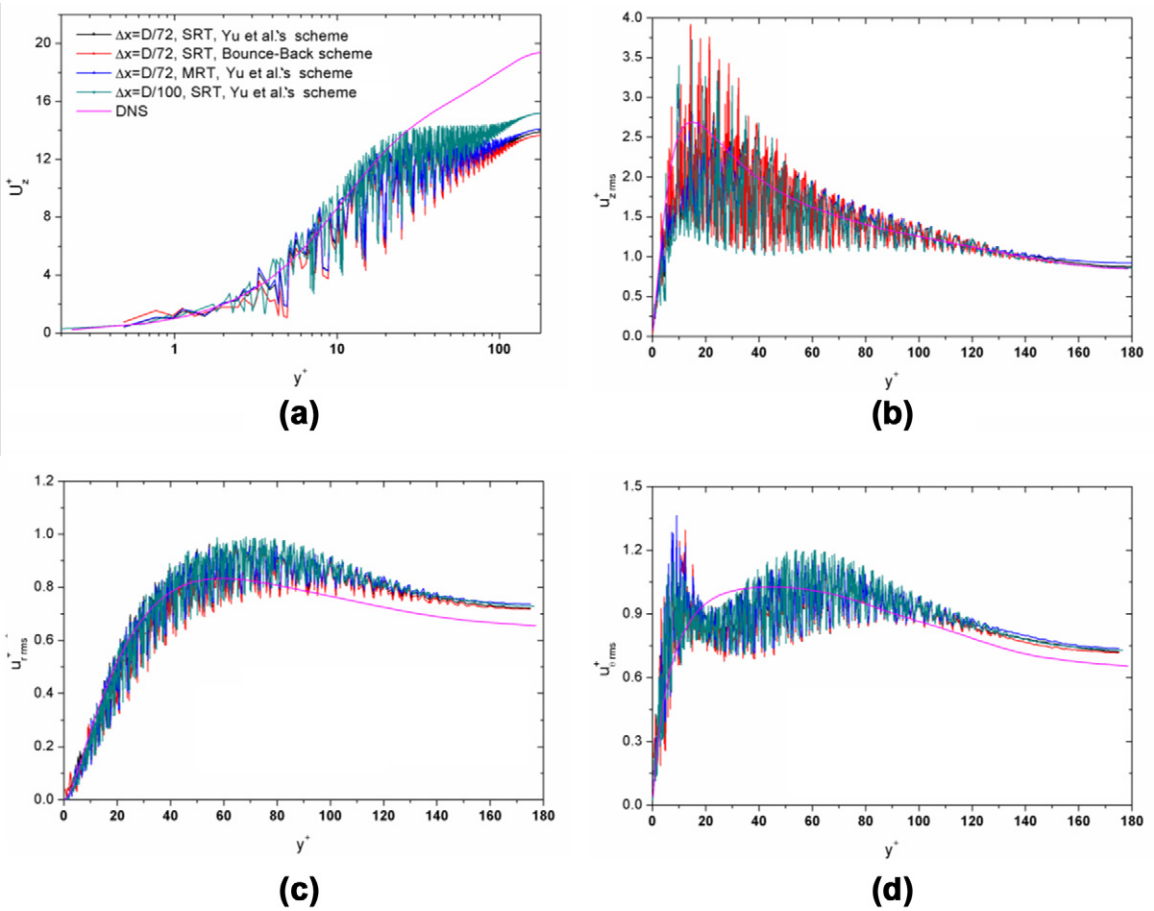

Fig. 7. (a) Streamwise mean velocities and (b) streamwise, (c) radial, and (d) azimuthal RMS fluctuation velocities obtained from the D3Q19 lattice model.

On average, the streamwise RMS velocity is under-predicted near the wall (below $y^+ \sim 90$) but is close to the DNS data in the core region [Fig. 7(b)]. The radial RMS velocity is, on average, under-estimated near the wall (below $y^+ \sim 50$) but over-estimated in the core region [Fig. 7(c)]. The axial and radial RMS velocity profiles show similar trends with those from the DNS on average, while the azimuthal RMS velocity profile shows a different shape from that of the DNS. This has higher val-ues in the viscous sublayer, lower values in the buffer layer, and higher values in the core region [Fig. 7(d)]. This is closely
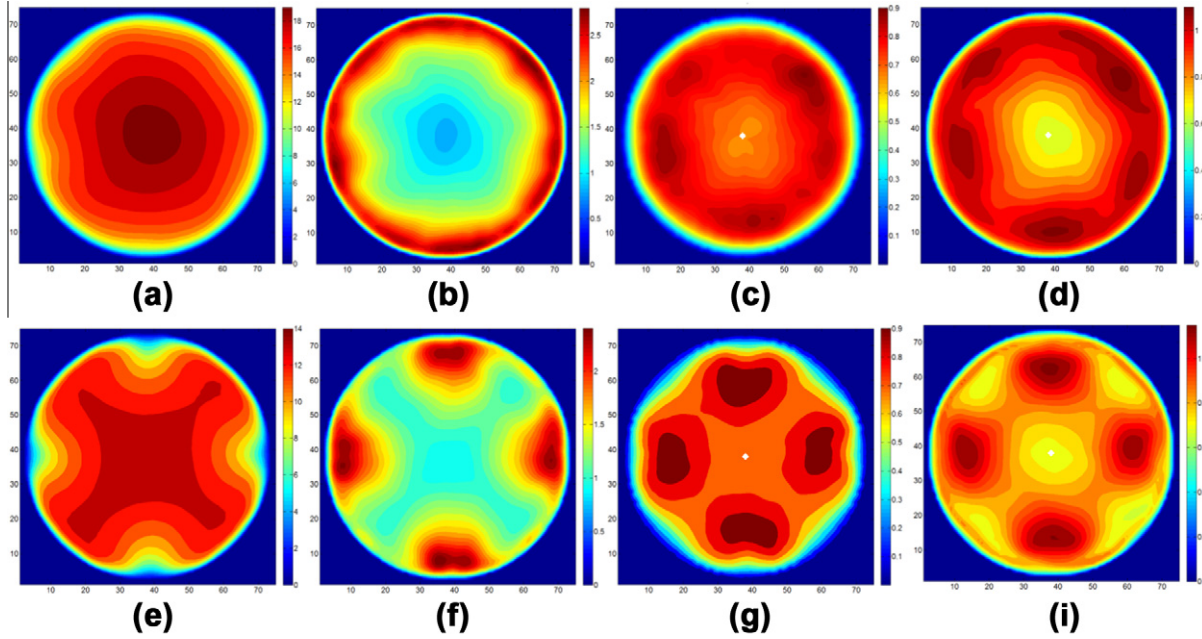
Fig. 8. Contour plots of U_z^+ [(a) and (e)], $u_{z,rms}^+$ [(b) and (f)], $u_{r,rms}^+$ [(c) and (g)] and $u_{\theta,rms}^+$ [(d) and (h)]) on cross-sectional planes obtained from D3Q27 lattice model [(a)–(d)] and D3Q19 lattice model [(e)–(h)] with grid size of $\Delta x = D/72$.

related to the strong secondary flows along the wall in the near-wall region between *Planes V* and *H* and *Planes D1* and *D2*, as will be discussed later.

The replacement of the solid boundary treatment with bounce-back scheme (red[1] lines) makes the under-prediction of the streamwise mean velocity even worse (from 28% to 30% at the center) and produces the RMS velocities similar to the case with Yu et al.'s scheme as in the D3Q27 lattice model [Fig. 6(a)].

In addition, to confirm that these large discrepancies from the DNS data are not due to the use of the SRT collision operator, we also considered the MRT collision operator. The numerical parameters for the MRT collision model are the same as those used in Premanath et al.'s [7] turbulent channel flow simulation. The under-estimation of the streamwise velocity in the core region is slightly improved (from 28% to 27% at the center), but the entire trend is still almost the same (blue lines) with other cases. The RMS velocities are also almost the same.

The higher resolution of $\Delta x = D/100$ relieves the under-estimation of the streamwise velocities (from 28% to 22% at the center), but it does not change the trend of the profiles of the standard case (dark cyan lines).

For all first- and second-order turbulence statistics considered, the profiles have much bigger oscillations than those obtained from the D3Q27 lattice model. This means that the rotational invariance is not achieved in terms of long-time-averaged turbulence statistics under the D3Q19 lattice model. This can be confirmed by the contour plots of turbulence statistics on the cross-section plane (Fig. 8). The contours obtained from the D3Q19 lattice model clearly show a certain preference in the circumferential direction. The streamwise mean velocities [Fig. 8(e)] are lower around the *Planes V* and *H* and higher around the Planes *D1* and *D2*. On the contrary, the RMS velocities [Fig. 8(b)–(d)] are higher around the *Planes V* and *H* and lower around the *Planes D1* and *D2*. The D3Q27 lattice model [Fig. 8(e)–(h)] does not show such a clear preference in the circumferential direction.

To clarify the reason for these trends of turbulence statistics under the D3Q19 lattice model, we added the radial profiles of turbulence statistics averaged over the *Planes D1* and *D2* and *Planes V* and *H*, respectively, to those under the standard case, as can be seen in Fig. 9. The RMS velocity profiles [Fig. 9(b)–(d)] obtained from averaging over the *Planes D1 and D2* always constitute the lower bounds of those from the average over the corresponding entire planes. This means that the defective planes could not properly transport flow information, thus producing consistently less turbulence than other planes. This explanation is consistent with White and Chong's [14] hypothesis that the defective planes (i.e., planes consisting of lattices with five velocity vectors) cause the rotational invariance to break. On the other hand, the RMS velocity profiles averaged over the *Planes V* and *H* do not always constitute the upper bounds, especially near the wall. This was also observed in Fig. 8(f)–(h).

Under the D3Q19 lattice model, the consistent, low turbulence fluctuations occur on four defective planes along the circumferential wall, while away from the defective planes, stronger turbulence production exists. This unbalanced turbulence

---

[1] For interpretation of color in Figs. 6 and 7, the reader is referred to the web version of this article.
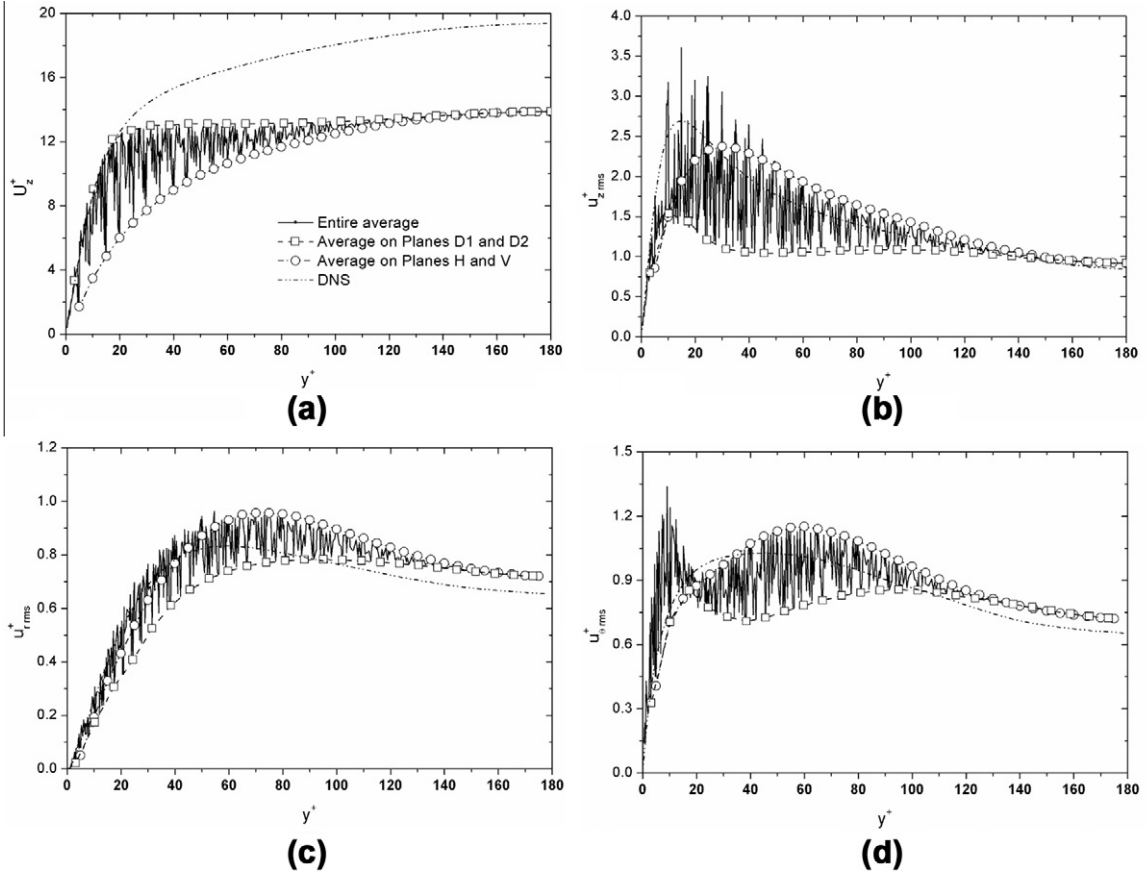
Fig. 9. (a) Streamwise mean velocities, (b) streamwise, (c) radial, and (d) azimuthal RMS velocities calculated from the averages over all and specific planes under the D3Q19 lattice model with grid size of $\Delta x = D/72$.

fluctuation due to the defective planes produce symmetric, four couples of counter-rotating turbulent secondary flows, as can be seen in Fig. 10(b). The strong ejections along the walls away from the defective planes promote a relatively low streamwise velocity near the *Planes V* and *H* (with the maximum distance from the defective planes), compared to the streamwise velocity at the defective planes, explaining the distorted isovels in Fig. 8(e) and streamwise mean velocities along the *Planes V* and *H* and *Planes D1* and *D2* in Fig. 9(a). The maximum secondary flow occurring near the wall away from each defective plane reaches about 9% of the mean centerline velocities under the D3Q19 lattice model. This also explains the under-estimation of streamwise flows under the D3Q19 lattice model. The similar patterns consisting of eight vortices are consistently observed for other D3Q19 lattice model cases considered in Fig. 7; i.e., with the MRT collision operator, higher resolution, and the bounce-back scheme, respectively. On the other hand, as can be seen in Fig. 10(a), no regular secondary flows, as in Fig. 10(a), are observed, and the maximum cross-flow is less than 1% of the mean centerline velocities under the D3Q27 lattice model.

4. Turbulent square duct flows

In the previous simulation of the turbulent circular pipe flow, we did not need to rotate the geometry to check the rotational invariance for the long-time-averaged turbulence statistics due to the circular pipe's axisymmetry; i.e., the rotational symmetry with respect to any angles. However, for the other internal flows like the square duct flows, the rotations of the geometry are required to confirm the rotational invariance. For the square duct with the rotational symmetry with respect to 90°, the geometry rotations about a center with arbitrary angles from 0° to 90° need to be performed to prove the rotational invariance. Since we cannot practically consider all angles from 0° to 90°, in this section we only consider two different grid sets, as shown in Fig. 11. In the *grid set A* [Fig. 11(a)], we locate the lateral boundaries to be aligned with grids as in [5]; thus, the defective planes match the corner bisectors of the square duct.

On the other hand, in the *grid set B* [Fig. 11(b)], we rotate the square geometry counter-clockwise by 45° about a channel center. Now the defective planes match the wall bisectors of the square duct. This figure also indicates the coordinate systems used in the presentation of the results.
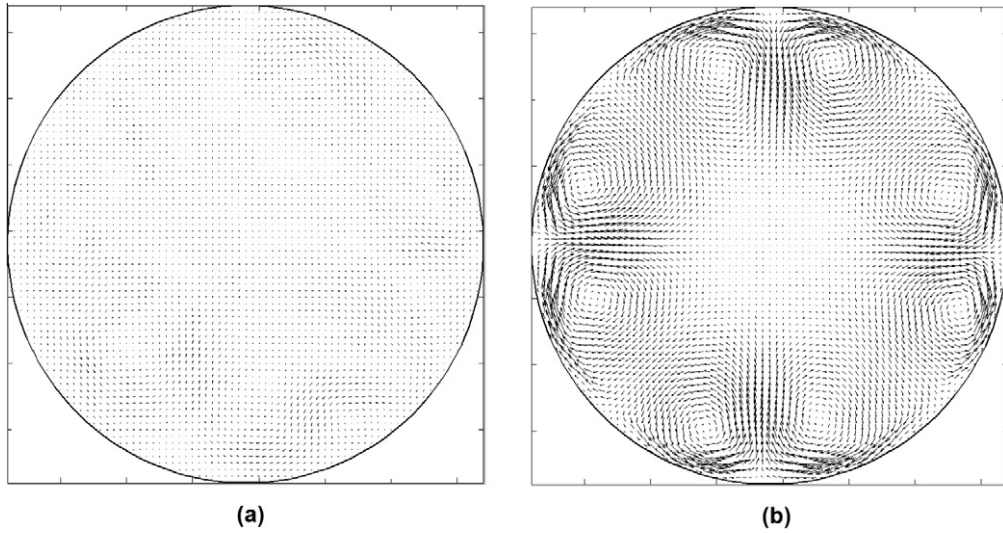
Fig. 10. Mean cross-flow vector fields obtained from (a) D3Q27 and (b) D3Q19 lattice models with grid size of $\Delta x = D/72$.

We consider the turbulent flows in a square duct with Re_τ ($=u_\tau W/\nu$) = 300, where W is the square duct width. The geometry is set to $W(x) \times W(y) \times 6W(z)$. For the *grid sets A and B*, grid sizes of $\Delta x = W/72$ and $W/71.4178$ are used, respectively. In the *grid set B*, we adjust the grid resolution such that the edge points are located between two nodes for the convenience of the post-processing. The external force density term corresponding to the pressure gradient is determined by $\bar{\tau}_w = \rho_0 u_\tau^2 = -\frac{1}{4} W dP/dz$. For the no-slip boundary condition on the four lateral wall boundaries, the halfway bounce-back scheme and Yu et al.'s scheme are applied to *grid sets A and B*, respectively. The Smagorinsky SGS model (with $C_S = 0.1$), with van Driest damping, is used as in the simulation of turbulent circular pipe flows. We also consider the MRT collision operator under the D3Q19 lattice model and adopt the parameters of Pattison et al. [5].

The turbulence statistics are calculated by time-averaging over 10 $t*$($= W/u_\tau$) and spatial-averaging, first along the streamwise direction, and then over four quadrants or eight octants [5,19]. The DNS data in [19] are used as reference data for the turbulent square duct flow. All velocity scales used in the presentation of the results are normalized by the average friction velocity u_τ.
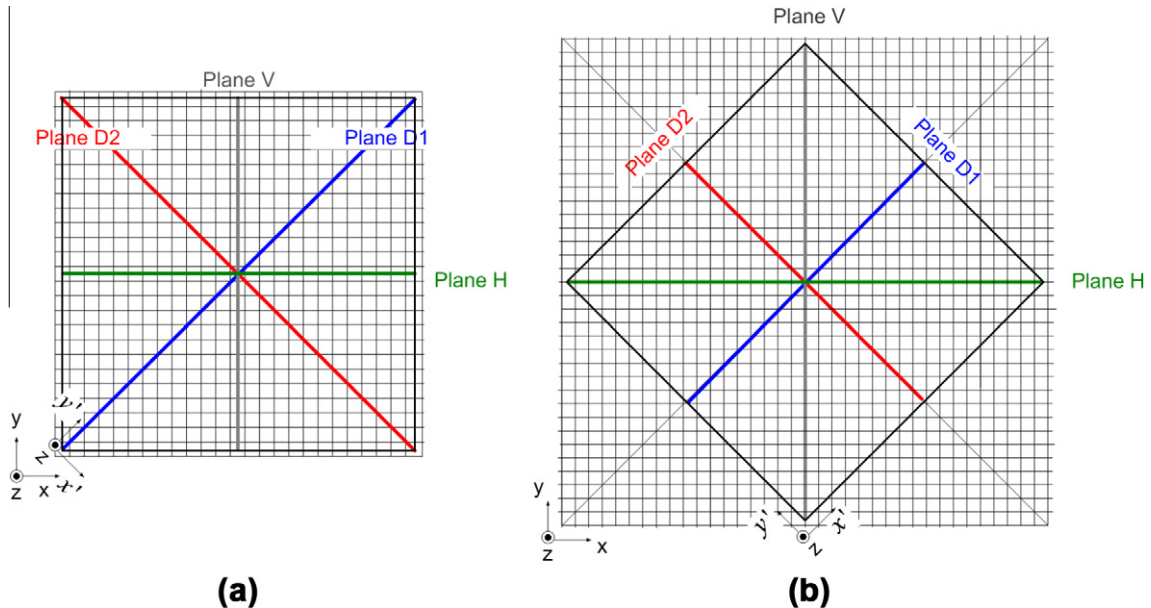

Fig. 11. Two different grid sets for the square channel flow simulation: (a) *grid set A* and (b) *grid set B*.
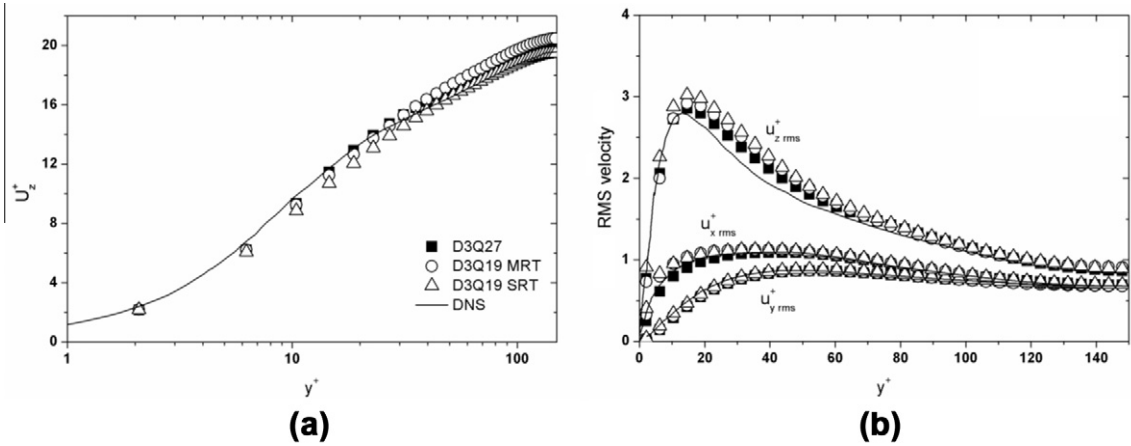
Fig. 12. Quadrant-averaged turbulence statistics along the wall bisector (*Planes V* and *H*) under the *grid set A*: (a) streamwise mean velocities and (b) RMS velocities.

First, we start with the results under the *grid set A*, where the coordinate systems in Fig. 11(a) are used. Fig. 12 shows the quadrant-averaged streamwise velocity and RMS velocities along the wall bisector in the *grid set A*. The D3Q19 and D3Q27 lattice models show overall similar results, although there are slight over-predictions of streamwise mean velocities and streamwise and spanwise RMS velocities under the D3Q27 lattice model and the D3Q19 lattice model with the MRT collision operator and the D3Q19 lattice models with the SRT and MRT collision operators, respectively.

Although the reasonable agreement of turbulence statistics along the wall bisector between two lattice models is shown in Fig. 12, we cannot conclude that the lattice model effect on the square duct flows is trivial under the *grid set A* because the defective planes are located on the corner bisectors, not the wall bisectors.

Fig. 13 presents the eight-octant-averaged, mean cross-flow velocity vector fields superimposed by the isovels of the streamwise mean velocity. In general, in the turbulent square duct flows, turbulent secondary flows are induced by the unbalanced turbulence fluctuation due to the existence of the corner region. A pair of counter-rotating vortices at each corner, i.e., one secondary vortex at each octant, exists [19,20]. The D3Q27 model [Fig. 13(a)] generates such a large secondary vortex in the octant cross-stream plane. This is consistent with those from other DNS [19,21] and LES [22] calculations. The distortion of isovels toward the corner due to the momentum transfer by the secondary velocities toward the corner is also observed. On the other hand, in the D3Q19 model with the MRT [Fig. 13(b)] and SRT [Fig. 13(c)], we can observe not only the large secondary vortex but also an additional small counter-rotating vortex (red circles), which is also observed in Pattison et al.'s [5] D3Q19 MRT-LBE simulation.

This additional small counter-rotating secondary flow observed only in the D3Q19 lattice model may be due to the defective planes matching the corner bisectors. The defective momentum transfer on the defective planes under the D3Q19 lattice model hampers the cross-flows toward the corner from the core along the corner bisector and reduces the distortion of
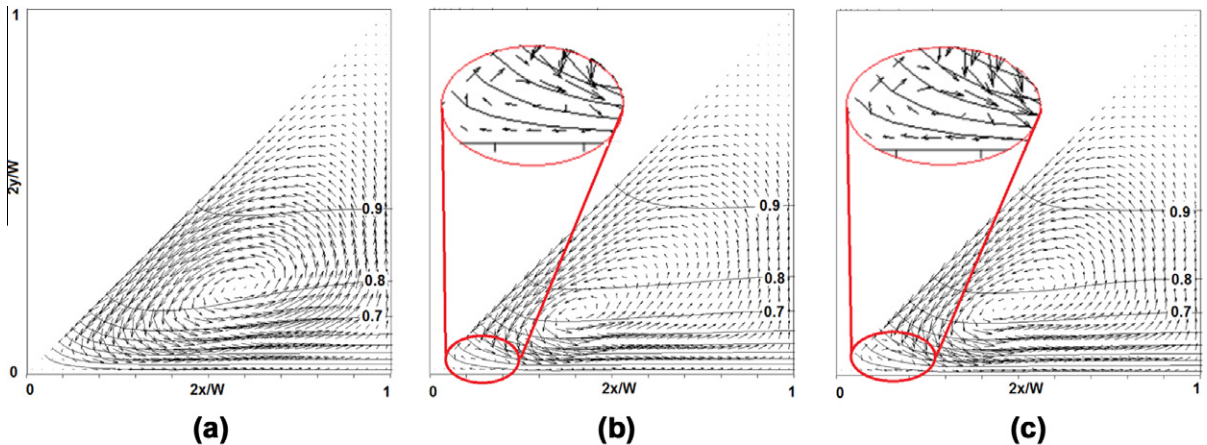

Fig. 13. Octant-averaged cross-flow vectors and streamwise velocity isovels (normalized by the centerline velocity) obtained from (a) D3Q27 lattice model, (b) D3Q19 lattice model with the MRT collision operator, and (c) D3Q19 lattice model with the SRT collision operator under the *grid set A*.
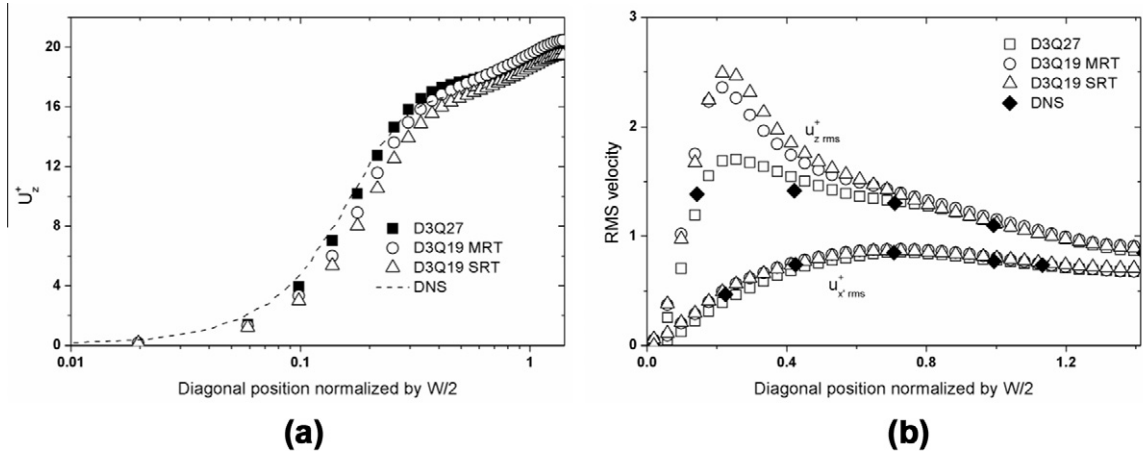
Fig. 14. Quadrant-averaged turbulence statistics along the wall bisector (*Planes D1* and *D2*) under the *grid set A*: (a) streamwise mean velocities and (b) RMS velocities.

streamwise isovels toward the corner. This instigates the ejections toward the core from the corner along the corner bisector, and this cross-flow collides with cross-flow from the core near the corner [between $(2x/W, 2y/W) = (0.1, 0.1)$ and $(0.2, 0.2)$], generating a small counter-rotating secondary vortex. The maximum secondary velocities (1.9–2.0% of the bulk velocity) occur just outside the wall viscous sublayer ($2y/W = 0.07$) for all cases, while the x-positions under the D3Q19 lattice model are closer to the corner ($2x/W = 0.36$ and 0.35 for the MRT and SRT collision operators, respectively) than the D3Q27 lattice model ($2x/W = 0.47$) and the DNS ($2x/W = 0.45$), due to the existence of the small secondary vortex under the D3Q19 lattice model.
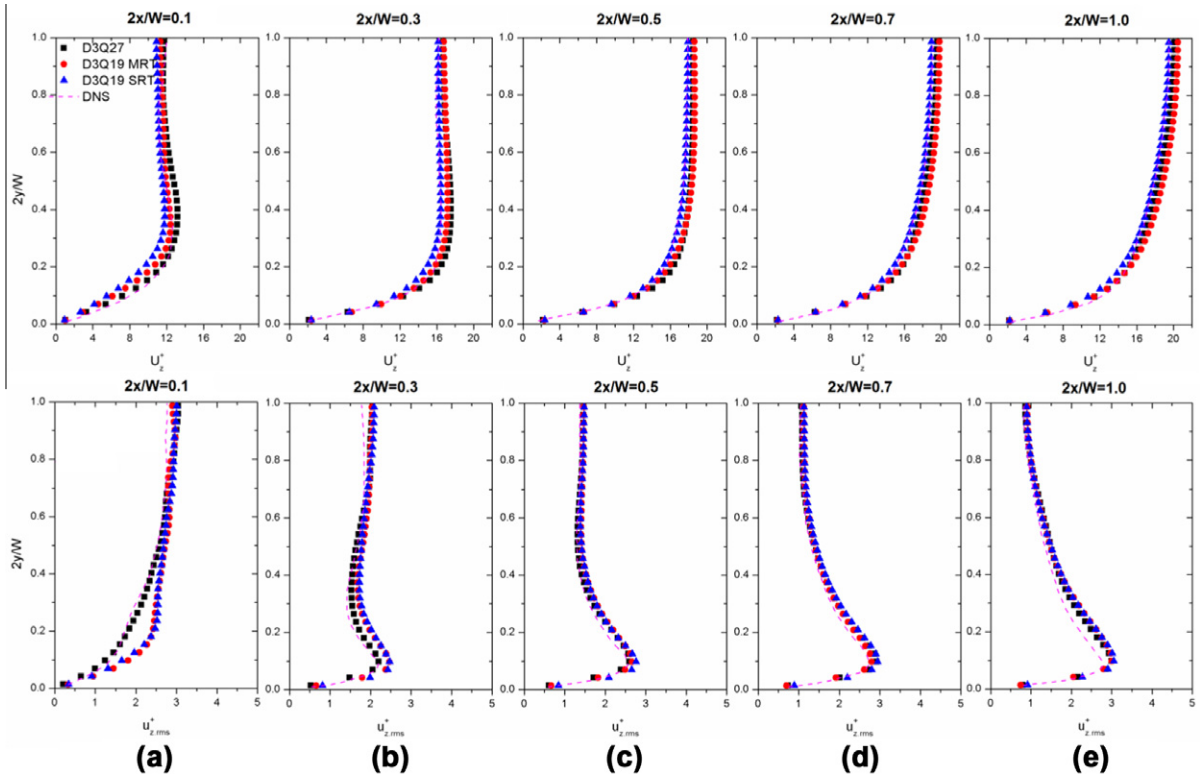

Fig. 15. Quadrant-averaged, streamwise mean (upper) and RMS (lower) velocity profiles along the wall-normal direction at (a) $2x/W = 0.1$, (b) $2x/W = 0.3$, (c) $2x/W = 0.5$, (d) $2x/W = 0.7$, and (e) $2x/W = 1.0$ under the *grid set A*.
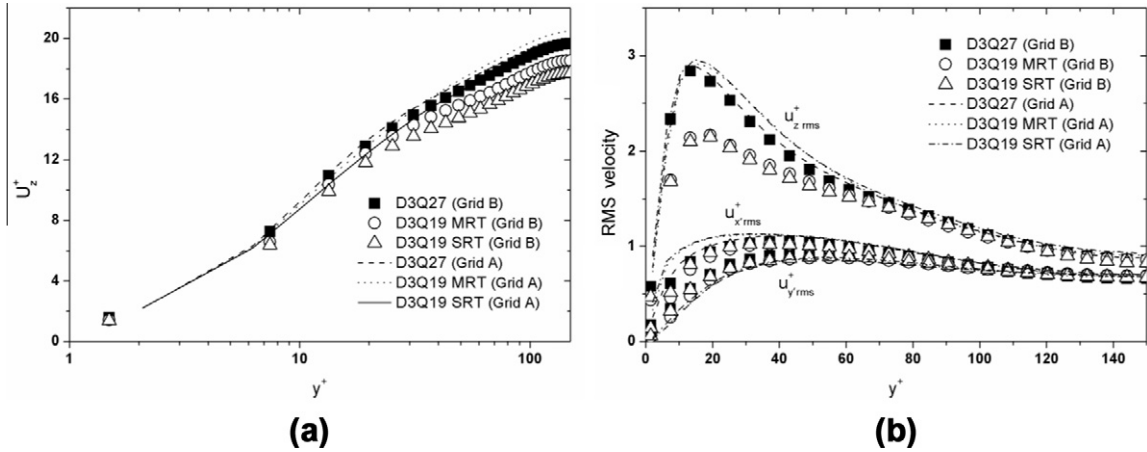
Fig. 16. Quadrant-averaged turbulence statistics along the wall bisector (*Planes D1* and *D2*) under the *grid set B*: (a) streamwise mean velocities and (b) RMS velocities.

Fig. 14 presents the streamwise mean velocities and RMS velocities along the corner bisector. The effect of the defective planes under the D3Q19 lattice model discussed in Fig. 13 also explains the under-estimation of the streamwise velocity near the corner and over-prediction of axial RMS velocities (near the region where counter-rotating secondary vortices collide with each other) under the D3Q19 lattice model. On the other hand, the D3Q27 lattice model shows good agreement with the DNS data.

Fig. 15 shows the streamwise mean and RMS velocity profiles along the wall-normal direction at different spanwise positions. This figure presents the effect of the defective planes on the entire flow field. As can be seen in Fig. 15, closer to the wall bisector [from (a) to (e)], the discrepancies of streamwise mean and RMS velocities near the corner between two lattice models become smaller. The discrepancies near the corner [Fig. 15(a) and (b)] were due to the defective planes as discussed in Figs. 13 and 14. The relatively small effect of the defective planes on the remaining flow field under the *grid set A* may be due to the positions of the planes on the corner confined by two walls. As will be discussed later, under the *grid set B* where the diagonal planes match the wall bisectors, the effect is more pronounced due to open positions of the defective planes.

Now we consider the results under the *grid set B* where the coordinate systems in Fig. 11(b) are used in the result presentation. Fig. 16 shows the turbulence statistics along the wall bisector calculated under the *grid set B* [*Planes D1* and *D2* in Fig. 11(b)]. For the D3Q27 lattice model, the turbulence statistics remain almost the same as that in *grid set A*, while for the D3Q19 lattice model, the streamwise mean velocity and the streamwise and transverse RMS velocities are markedly lowered compared to *grid set A*. Under the D3Q19 lattice model with SRT and MRT collision operators, the centerline streamwise velocities in the *grid set B* are about 10% lower than those in the *grid set A*. These underestimations are similar to those on defective planes under the D3Q19 lattice model in the simulation of turbulent circular pipe flows. In addition, these underestimations are not due to the grid resolution lowered in the diagonal planes, since the D3Q27 lattice models show little change between two grid sets.
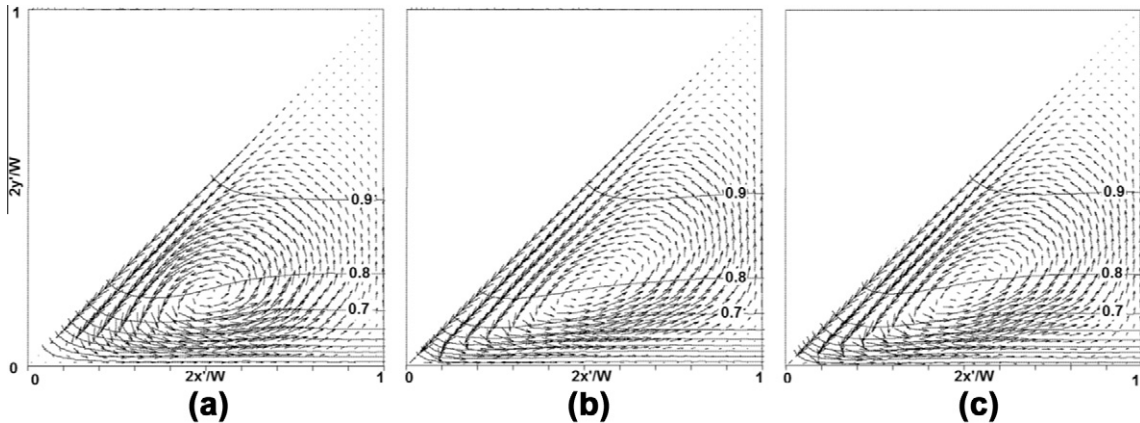

Fig. 17. Octant-averaged cross-flow vectors and streamwise velocity isovels (normalized by the centerline velocity) obtained from (a) D3Q27 lattice model, (b) D3Q19 lattice model with the MRT collision operator, and (c) D3Q19 lattice model with the SRT collision operator under the *grid set B*.
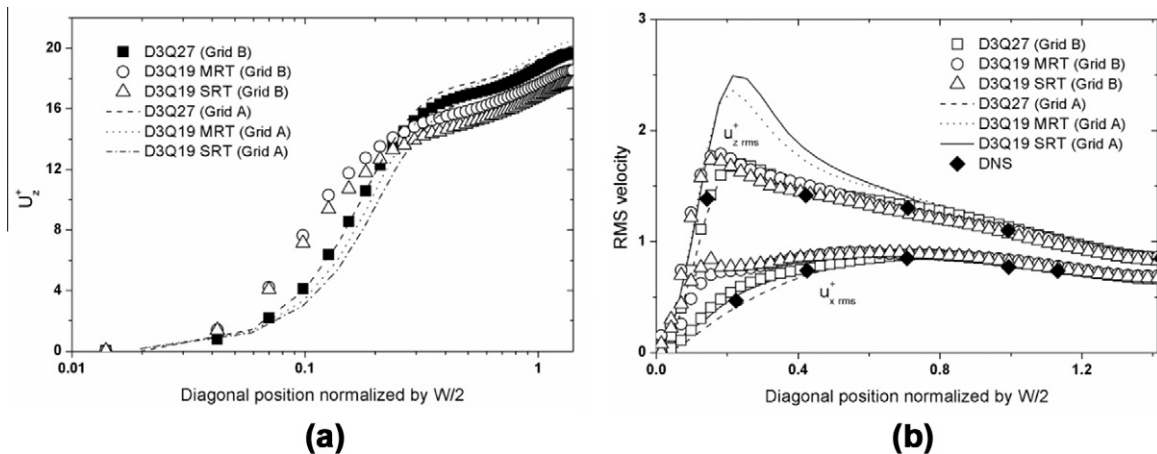
Fig. 18. Quadrant-averaged turbulence statistics along the corner bisector (*Planes V and H*) under the *grid set B*: (a) streamwise mean velocities and (b) RMS velocities.

As can be seen in Fig. 17, the D3Q19 lattice models no longer have a small additional counter-rotating secondary vortex in the eight-octant-averaged, mean cross-flow vector field because the defective planes are not located on the corner bisectors under the *grid set B*; thus, the cross-flows toward the corner along the corner bisectors are no longer hampered. Rather, due to the reduced turbulence fluctuation near the wall bisector, the ejections away from the corner are less promoted, thus causing the deeper penetration of the cross-flow toward the corner and stronger secondary flows compared to those from the D3Q27 lattice model and the DNS. For the penetration, the intersection points between the corner bisector and the iso-vels of 0.7 and 0.8 are (0.17, 0.17) and (0.23, 0.23) for the D3Q27 lattice model, while (0.14, 0.14) and (0.21, 0.21) and (0.14, 0.14) and (0.22, 0.22) for the D3Q19 lattice model with MRT and SRT collision operators. The magnitude of the maximum

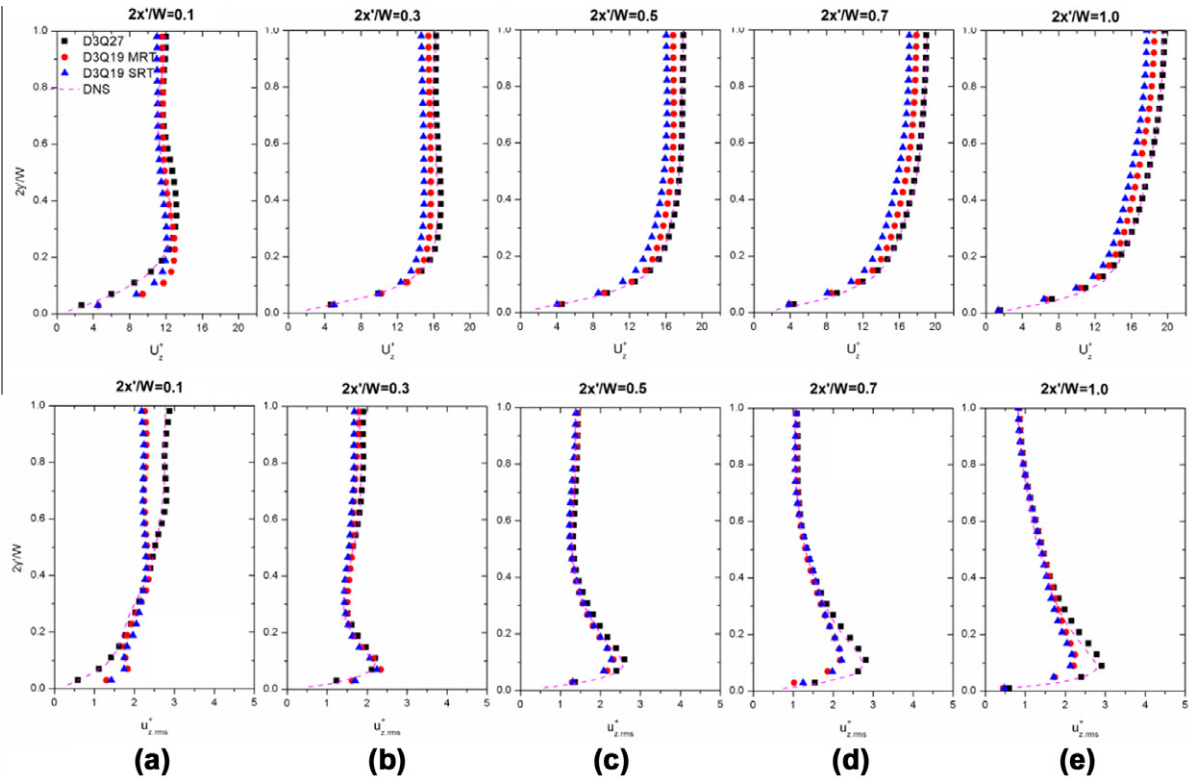
Fig. 19. Quadrant-averaged, streamwise mean (upper) and RMS (lower) velocity profiles along the wall-normal direction at (a) $2x'/W = 0.1$, (b) $2x'/W = 0.3$, (c) $2x'/W = 0.5$, (d) $2x'/W = 0.7$, and (e) $2x'/W = 1.0$ under the *grid set B*.

secondary velocity is 3.7% of the bulk velocity under the D3Q19 lattice model, while 2.0% and 1.9% in the D3Q27 lattice model and the DNS, respectively.

Fig. 18 shows the quadrant-averaged turbulence statistics along the corner bisector [*Planes H* and *V* in Fig. 11(b)]. For the D3Q27 lattice model, the difference between two grid sets is very small. On the other hand, for D3Q19 lattice model, the streamwise velocity is over-predicted near the wall, as discussed in Fig. 17(b) and (c) and under-predicted in the core region, as discussed in Fig. 16(a). The discrepancies of the streamwise RMS velocities between two models become small because no additional counter-rotating secondary vortex exists under the grid set B. On the other hand, the discrepancies of the spanwise RMS velocities between two models become larger due to deeper penetration of the cross-flows toward the corner.

Fig. 19 shows streamwise mean and RMS velocity profiles along the wall-normal direction at different spanwise positions under the *grid set B*. The D3Q27 lattice model under the *grid set B* provides results similar to those from the same lattice model under *grid set A* when compared to Fig. 15 and results more comparable to the DNS. This will be discussed further in Section 5. On the other hand, the D3Q19 lattice model shows large discrepancies between two grid sets when compared to Fig. 15 and shows much worse agreement with the DNS data. This may be because the effect of the defective planes under the *grid set A* is restricted to the corner region due to the geometrical confinement of the corner, while under the *grid set B*, the defective planes are not confined; thus, they are more influential to the entire flow field.

5. Discussion

In the previous two sections, we provided the simulation results of the wall-bounded turbulent flows in two geometries – a circular pipe and a square duct with and without 45°-rotation – to investigate the effect of lattice models in the LBM.

In the circular straight pipe geometry, when the flow was laminar (Re = 500), it had the rotational invariance for both D3Q19 and D3Q27 lattice models. The position corresponding to L_∞-error was not on the defective planes in the D3Q19 lattice model. This means that the planes consisting of the lattices with five velocities can properly transport the flow information when the flow is aligned with lattice velocity vectors $\mathbf{e}_5$ and $\mathbf{e}_6$ in Fig. 3. This is consistent with White and Chong's [14] results.

When the flow was fully turbulent in the same straight circular pipe, the rotational invariance in terms of the turbulence statistics was still maintained under the D3Q27 lattice model, whereas it was broken under the D3Q19 lattice model. The broken rotational invariance could be attributed to the effect of the defective planes because the consistent minimum turbulence fluctuations along the defective planes induced the strong turbulent secondary flows, thus distorting the entire statistical flow pattern. This is different from White and Chong's [14] study in terms of the source causing the breaking of the rotational invariance. In their study, the rotational invariance of the flow was broken downstream of a sudden expansion because the defective planes could not properly transport the complex flow behaviors, such as impingements and reverse flows. In other words, the source revealing the effect of the defective planes was flow due to geometrical changes along the streamwise direction in White and Chong [14], while, in our case, the source was the naturally occurring turbulence due to instability of wall-bounded flows without geometrical change.

In the simulation of the turbulent square duct flows, to see the effect of the defective planes, we considered two grid configurations, where defective planes were located on the wall bisectors and the corner bisectors, respectively. From the former grid configuration (*grid set A*), we found the deficiency of the D3Q19 lattice model by investigating the turbulence statistics and secondary flow structures near the corner. Due to the deficiency of the momentum transfer along the corner bisector matching the defective planes, the penetration of the cross-flows toward the corner from the core, i.e., the occurrence of the turbulence vortices near the corner bisector, was reduced. This led to the early separation to two counter-rotating vortices against the corner bisector line and small, additional counter-rotating vortices at the corner only under the D3Q19 lattice model. On the other hand, the turbulence statistics along the wall bisectors (matching *Planes V* and *H*), and in other regions away from the corner, did not show big discrepancies from those from the D3Q27 lattice model and the DNS data. This means that the effect of the defective planes under the former grid configuration is restricted to the corner region to a degree due to the geometrical confinement of the corner.

For the latter grid configuration (*grid set B*), the deficiency of the D3Q19 lattice model was more clearly observed. First, the D3Q19 lattice model showed remarkable differences of the first- and second-order turbulence statistics between the former and the latter grid configurations, while the D3Q27 lattice model showed similar results. This means that the D3Q19 lattice model does not have the invariance of 45° rotation. Second, the D3Q19 lattice model under the latter grid configuration showed more discrepancies from the DNS data in the turbulence statistics for overall fluid domain than under the former grid configuration, although additional small counter-rotating secondary vortices in the former grid configuration were removed. This was because the effect of the defective planes was influential to the entire flow fields due to their open positions; i.e., not corner locations but open wall bisector locations. On the other hand, the D3Q27 lattice model could produce results comparable to DNS data for both grid configurations.

Another interesting thing found in this study is the improvement of the accuracy in the D3Q27 lattice model under the grid configuration with non-uniform wall normal distances. In the turbulent pipe flows, where the wall-normal distances change with circumferential locations, even with low resolution $\Delta x = D/60$, quite accurate results could be obtained. Also, in the square duct flows with a 45°-rotated grid configuration with non-uniform wall-normal distances (*grid set B*), we could obtain the results more comparable to the DNS data than with a grid configuration without a rotation with uniform

wall-normal distances (*grid set A*). This may be due to finer effective scales in the wall normal direction under the grid with non-uniform wall-normal distances. For example, for the *grid set A* in square duct flows [Fig. 11(a)], wall-normal grid positions start at $y^+ = 2.083$ (i.e., $0.5\Delta x^+$) and increase by 4.167 (i.e., $1\Delta x^+$) in the wall unit for all starting spanwise coordinates. In the *grid set B* [Fig. 11(b)], wall-normal grid positions start alternately at $y^+ = 1.485$ (i.e., $\sqrt{2}/4\Delta x^+$) and $y^+ = 4.455$ (i.e., $3\sqrt{2}/4\Delta x^+$) and increase by 5.941 (i.e., $\sqrt{2}\Delta x^+$) in the wall unit. Therefore, in *the grid set B*, the wall-normal grid size over neighboring two grid points in the spanwise direction with distance of 2.970 in the wall unit becomes 2.970 in wall unit, which is 71% of the wall-normal grid size under the grid set A. This finer grid resolution in the wall-normal direction is expected to resolve the smaller turbulence scale especially in the buffer layer, thus relieving over-estimations of the streamwise mean and RMS velocities (see Figs. 15 and 19). For circular pipe flows, the effective wall-normal grid size is much finer, although the circumferential grid size becomes larger.

It should also be pointed out that, in this study, we adopted only the Smagorinsky model with fixed coefficient ($C_S = 0.1$) together with van Driest damping and did not show the effect of the turbulence model. This is because, in the preliminary calculation, the results using different coefficients ($C_S = 0.12$ and 0.17) under the Smagorinsky SGS model and other SGS models, like the WALE SGS model [8], did not change our main results and conclusions about the lattice model effect obtained from the Smagorinsky SGS model with $C_S = 0.1$. However, since the results without van Driest damping under the Smagorinsky SGS model showed big discrepancies (for example, 5% under-estimation of the streamwise mean velocity under the $\Delta x = D/60$ for the turbulent pipe flows) from the other calculations and the DNS data, we consistently included it.

In addition, in the simulation of the turbulent square channel flows, we used the constant average friction velocity for the van Driest damping, although the local friction velocity changes along the lateral wall of the square duct. The calculation using the WALE SGS model not affected by local friction velocity showed the better agreement with the DNS results. For example, with the D3Q27 lattice model under the grid set A, its secondary vortex position became closer to the DNS result of [19], and the over-prediction of the mean centerline streamwise velocity was reduced to 1.2% from 2.7%. However, the main characteristics of turbulence structures, flow patterns, and turbulence statistics obtained from the model addressed in this study did not change.

The D3Q27 lattice model produced more accurate results than the D3Q19 lattice model in the turbulent flows in the square duct and circular pipe flows, while the D3Q27 lattice model required about 30% more CPU time and memory than the D3Q19 lattice model for the same SRT collision operator calculation. It is clear that the efficiency in the D3Q19 lattice model cannot justify the use of it in the turbulent circular pipe flows and turbulent square duct flows under the *grid set B*, where the flow is clearly distorted and the turbulence statistics have large discrepancies. However, if, as in near the wall bisector region under the *grid set A* for the turbulent square duct flows, the range of interest is confined to the region where the distortion of the flow and turbulence statistics are small, we may be able to adopt the D3Q19 lattice model. However, the use of the D3Q19 lattice model in turbulent wall-bounded flows should be avoided until it is confirmed that the effect of the defective planes is negligible in the region of interest. Since the validation data are not available for most complex flow problems, we may always have to perform the comparison between D3Q19 and D3Q27 lattice models to justify the use of the D3Q19 lattice model.

6. Conclusions

In this study, we investigated the effect of the 3D lattice models (D3Q27 and D3Q19 lattice models) in the LBM for turbulent wall-bounded flows – turbulent circular pipe and square duct flows. In the simulation of the turbulent circular pipe flow, the D3Q27 lattice model showed the rotational invariance in terms of the turbulence statistics and could produce the first and second-order turbulence statistics comparable to DNS data. On the other hand, in the D3Q19 lattice model, the consistent, unbalanced turbulence fluctuation on the defective planes, i.e., planes consisting of lattices with five velocity vectors, drove the systematic, strong turbulent secondary flows, thus breaking the rotational invariance and generating the unreasonable results.

In the simulation of the turbulent square duct flows, the D3Q27 lattice model showed the invariance before and after 45° grid rotation, while the D3Q19 lattice model did not. The D3Q19 lattice model, under the grid configuration aligned with lateral boundaries (*grid set A*), produced the mean and second-order turbulence statistics similar to the DNS data in overall region, but it generated additional, small counter-rotating secondary vortices near the corner due to the defective planes matching the corner bisectors. After the 45° grid rotation (*grid set B*), the additional vortices were removed, but the entire flow statistics were deteriorated due to the defective planes matching the wall bisectors. On the other hand, the D3Q27 lattice model without such planes produced the first- and second-order turbulence statistics comparable to the DNS data in the entire region for both grid sets.

The broken rotational invariance and erroneous results under the D3Q19 lattice model could be consistently explained by the defective planes consisting of 2D lattices with five velocities under the D3Q19 lattice model, based on the White and Chong's [14] hypothesis. The defective planes consistently caused the problem in the momentum transfer on the planes, distorting the turbulence (vortex) structures near the planes, and thus, the entire turbulence statistics and flow pattern.

Thus, when simulating the turbulent flows inside the geometry (especially with a certain rotational symmetry) using the LBM, it is recommended to use the D3Q27 lattice model instead of the D3Q19 lattice model for obtaining consistently accurate results, although the D3Q27 model is more expensive in terms of CPU time and memory than the D3Q19 model.

In this study, we investigated the lattice model effect for the relatively low Reynolds turbulent wall-bounded flows and for only two geometries. We leave the investigation of the lattice model effect under the higher Reynolds turbulent wall-bounded flows and for other geometries, such as turbulent flows in a rod bundle and in a pipe with different shapes, to future studies. It should also be pointed out that since the D3Q27 lattice model is not also sufficiently Galilean invariant [23], it may lead to problems similar to the D3Q19 lattice model in the limited situations. In this case, the higher-order lattice models with more sufficient Galilean invariance, such as the D3Q41 lattice model [24], may need to be considered.

References

[1] D. Bespalko, A. Pollard, M. Uddin, Direct numerical simulation of fully-developed turbulent channel flow using the lattice Boltzmann method and analysis of OpenMP scalability, Lect. Notes Comput. Sci. 5976 (2010) 1–19.
[2] P. Lammers, K.N. Beronov, R. Volkert, G. Brenner, F. Durst, Lattice BGK direct numerical simulation of fully developed turbulence in incompressible plane channel flow, Comput. Fluids 35 (2006) 1137–1153.
[3] R.K. Freitas, A. Henze, M. Meinke, W. Schroder, Analysis of lattice-Boltzmann methods for internal flows, Comput. Fluids 47 (2011) 115–121.
[4] S. Jafari, M. Rahnama, Shear-improved Smagorinsky modeling of turbulent channel flow using generalized lattice Boltzmann equation, Int. J. Numer. Methods Fluids 67 (2011) 700–712.
[5] M.J. Pattison, K.N. Premnath, S. Banerjee, Computation of turbulent flow and secondary motions in a square duct using a forced generalized lattice Boltzmann equation, Phys. Rev. E 79 (2009) 026704.
[6] K.N. Premnath, M.J. Pattison, S. Banerjee, Dynamic subgrid scale modeling of turbulent flows using lattice-Boltzmann method, Physica A 388 (2009) 2640–2658.
[7] K.N. Premnath, M.J. Pattison, S. Banerjee, Generalized lattice Boltzmann equation with forcing term for computation of wall-bounded turbulent flows, Phys. Rev. E 79 (2009) 026703.
[8] M. Weickert, G. Teike, O. Schmidt, M. Sommerfeld, Investigation of the LES WALE turbulence model within the lattice Boltzmann framework, Comput. Math. Appl. 59 (2010) 2200–2214.
[9] G. Mayer, G. Hazi, Direct numerical and large eddy simulation of longitudinal flow along triangular array of rods using the lattice Boltzmann method, Math. Comput. Simulat. 72 (2006) 173–178.
[10] R. Mei, W. Shyy, D. Yu, L.S. Luo, Lattice Boltzmann method for 3-D flows with curved boundary, J. Comput. Phys. 161 (2000) 680–699.
[11] D. d'Humieres, I. Ginzburg, M. Krafczyk, P. Lallemand, L.S. Luo, Multiple-relaxation-time lattice Boltzmann models in three dimensions, Philos. Trans. Roy. Soc. A 360 (2002) 437–451.
[12] M. Geier, A. Greiner, J.G. Korvink, Cascaded digital lattice Boltzmann automata for high Reynolds number flow, Phys. Rev. E 73 (2006) 066705.
[13] J.G.M. Eggels, F. Unger, M.H. Weiss, J. Westerweel, R.J. Adrian, R. Friedrich, F.T.M. Nieuwstadt, Fully developed turbulent pipe flow: a comparison between direct numerical simulation and experiment, J. Fluid Mech. 268 (1994) 175–209.
[14] A.T. White, C.K. Chong, Rotational invariance in the three-dimensional lattice Boltzmann method is dependent on the choice of lattice, J. Comput. Phys. 230 (2011) 6367–6378.
[15] Z.L. Guo, C.G. Zheng, B.C. Shi, Discrete lattice effects on the forcing term in the lattice Boltzmann method, Phys. Rev. E 65 (2002) 046308.
[16] X.Y. He, L.S. Luo, Lattice Boltzmann model for the incompressible Navier–Stokes equation, J. Stat. Phys. 88 (1997) 927–944.
[17] D.Z. Yu, R.W. Mei, L.S. Luo, W. Shyy, Viscous flow computations with the method of lattice Boltzmann equation, Prog. Aerosp. Sci. 39 (2003) 329–367.
[18] P. Moin, J. Kim, Numerical investigation of turbulent channel flow, J. Fluid Mech. 118 (1982) 341–377.
[19] S. Gavrilakis, Numerical simulation of low-Reynolds-number turbulent flow through a straight square duct, J. Fluid Mech. 244 (1992) 101–129.
[20] A. Huser, S. Biringen, Direct numerical simulation of turbulent flow in a square duct, J. Fluid Mech. 257 (1993) 65–95.
[21] Y. Joung, S.U. Choi, J.I. Choi, Direct numerical simulation of turbulent flow in a square duct: analysis of secondary flows, J. Eng. Mech.-ASCE. 133 (2007) 213–221.
[22] M.S. Vazquez, O. Metais, Large-eddy simulation of the turbulent flow through a heated square duct, J. Fluid Mech. 453 (2002) 201–238.
[23] S.S. Chikatamarla, C.E. Frouzakis, I.V. Karlin, A.G. Tomboulides, Lattice Boltzmann method for direct numerical simulation of turbulent flows, J. Fluid Mech. 656 (2010) 298–308.
[24] S.S. Chikatamarla, I.V. Karlin, Lattices for the lattice Boltzmann method, Phys. Rev. E 79 (2009) 046701.